

This work was written as part of one of the author's official duties as an Employee of the United States Government and is therefore a work of the United States Government. In accordance with 17 U.S.C. 105, no copyright protection is available for such works under U.S. Law. Access to this work was provided by the University of Maryland, Baltimore County (UMBC) ScholarWorks@UMBC digital repository on the Maryland Shared Open Access (MD-SOAR) platform.






Please provide feedback

Please support the ScholarWorks@UMBC repository by emailing [scholarworks-group@umbc.edu](mailto:scholarworks-group@umbc.edu) and telling us what having access to this work means to you and why it's important to you. Thank you.

# Optical and mechanical design of a telescope for lunar spectral irradiance measurements from a high-altitude aircraft

Cite as: Rev. Sci. Instrum. **91**, 094505 (2020); <https://doi.org/10.1063/5.0004848>

Submitted: 14 February 2020 . Accepted: 25 August 2020 . Published Online: 09 September 2020

C. J. Zarobila , S. Grantham, S. W. Brown, J. T. Woodward , S. E. Maxwell , D. R. Defibaugh, T. C. Larason , and K. R. Turpie 



View Online



Export Citation



CrossMark

## ARTICLES YOU MAY BE INTERESTED IN

[Real-time laser Doppler anemometry for optical air data applications in low aerosol environments](#)

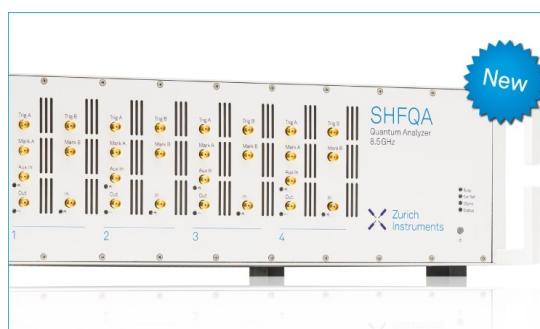
Review of Scientific Instruments **91**, 095106 (2020); <https://doi.org/10.1063/5.0014389>

[Site-selection criteria for the Einstein Telescope](#)

Review of Scientific Instruments **91**, 094504 (2020); <https://doi.org/10.1063/5.0018414>

[Monitoring the build-up of hydrogen polarization for polarized hydrogen-deuteride \(HD\) targets with nuclear magnetic resonance \(NMR\) at 17 T](#)

Review of Scientific Instruments **91**, 095104 (2020); <https://doi.org/10.1063/5.0005696>



## Your Qubits. Measured.

Meet the next generation of quantum analyzers

- Readout for up to 64 qubits
- Operation at up to 8.5 GHz, mixer-calibration-free
- Signal optimization with minimal latency

Find out more



# Optical and mechanical design of a telescope for lunar spectral irradiance measurements from a high-altitude aircraft

Cite as: Rev. Sci. Instrum. 91, 094505 (2020); doi: 10.1063/5.0004848

Submitted: 14 February 2020 • Accepted: 25 August 2020 •

Published Online: 9 September 2020



C. J. Zarobila,<sup>1,a)</sup> S. Grantham,<sup>1</sup> S. W. Brown,<sup>1</sup> J. T. Woodward,<sup>1</sup> S. E. Maxwell,<sup>1</sup> D. R. Defibaugh,<sup>1</sup> T. C. Larason,<sup>1</sup> and K. R. Turpie<sup>2</sup>

## AFFILIATIONS

<sup>1</sup>Sensor Science Division, National Institute of Standards and Technology, Gaithersburg, Maryland 20899, USA

<sup>2</sup>Joint Center for Earth Systems Technology, University of Maryland Baltimore County, Baltimore, Maryland 21250, USA

<sup>a)</sup>Author to whom correspondence should be addressed: zarobila@nist.gov

## ABSTRACT

We have designed a non-imaging telescope for measurement of the spectral irradiance of the moon. The telescope was designed to be integrated into a wing pod of a National Aeronautics and Space Administration ER-2 research aircraft to measure lunar spectral irradiance during flight. The telescope and support system were successfully flown in August 2018 at altitudes near 21 km and at speeds of ~760 km/h. The wing pod in which the telescope is mounted has an opening through which the moon can be observed. The mount exposes the telescope to high winds, low pressures, temperatures near  $-60^{\circ}\text{C}$ , and vibrations both due to flight and due to the motion of the aircraft on the ground. This required a telescope design with high thermal stability and high resistance to shock. The optical design of the telescope is optimized to have high throughput and spatially uniform transmission from 380 nm to 1000 nm over a field of view about three times the angular size of the moon as viewed from the Earth. The final design resulted in a telescope with singlet design incorporating a 139.7 mm lens with an effective focal length of 377 mm and a field of view of  $1.6^{\circ}$ . The light from the telescope is introduced into an integrating sphere, which destroys the image and the polarization for measurement by a fiber-coupled spectroradiometer. Herein, we present an overview of the instrument and support system with emphasis on the telescope design.

<https://doi.org/10.1063/5.0004848>

## I. INTRODUCTION

The moon is an important exo-atmospheric calibration target for space-based sensors that observe the Earth because the lunar surface is radiometrically stable, reflected solar flux levels approximate those from the Earth, and no atmospheric corrections need to be applied for the calibration. However, the current uncertainties<sup>1</sup> in the knowledge of the spectral irradiance of the moon, at the 3%–6% level in the visible to near infrared (VNIR) wavelengths, prevent the moon from being used as an absolute calibration source. Instead, it is used for sensor trending.

Knowledge of the lunar irradiance at the sub-2% level would make the moon a cost-effective alternative to ground-based vicarious calibration for on-orbit absolute calibration. Higher levels of precision in knowledge of the lunar irradiance, along with the

improvements in satellite calibration that the knowledge would enable, would result in more effective and rapid measurement of climate and weather changes as well as an improved ability to combine data from different satellite sensors.<sup>2</sup>

The National Institute of Standards and Technology (NIST) is pursuing two complementary pathways toward the goal of developing a new, precise, SI-traceable dataset of the lunar spectral irradiance. One pathway involves a set of ground-based measurements over a long period of time.<sup>3,4</sup> The other pathway is via a NIST- and National Aeronautics and Space Administration (NASA)-sponsored system that operates in the wing pod of an ER-2 aircraft that is part of NASA's Airborne Science Program. This latter system is known as the Airborne Lunar Spectral Irradiance system, or air-LUSI, and measures the lunar spectral irradiance in the VNIR region from an altitude of ~21 km. From this high altitude, atmospheric corrections

to at-sensor measurements are minimized. Details of the air-LUSI system and the full motivation are described in an upcoming paper.<sup>5</sup> For this project, NIST and its partners constructed a specialized telescope to collect light and direct it, independent of polarization, into a spectroradiometer. This paper describes the design and construction of that telescope and light collection system.

The telescope's design reflects the need for precise calibration. The field of view is restricted, and stray light is carefully controlled so that during calibration, only light from the calibration source enters the spectroradiometer and so that during flight, no light originating from the aircraft or reflecting from its surfaces affects the measurements. The materials used in construction are chosen so that calibration in a hangar that can reach temperatures exceeding 30 °C is valid when the telescope tube is exposed to ambient temperatures approaching -60 °C in the open wing pod of the ER-2. The dimensions, optical train, and light collection strategy are all chosen so that a calibration performed with a light source 15 m away is valid for a target at infinity.

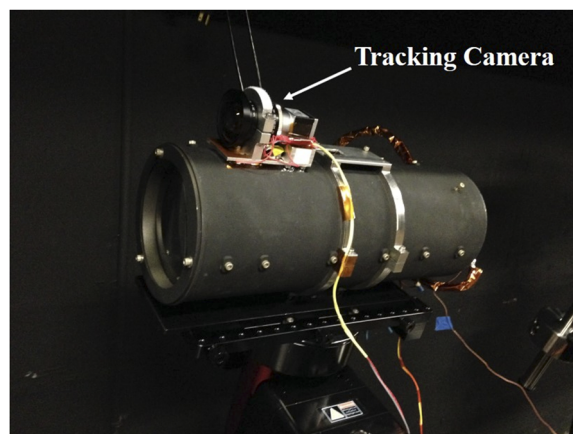
The telescope design also faces mechanical constraints. It must fit within the ER-2 wing pod and be small enough to be tilted up to near vertical and to yaw up to  $\pm 15^\circ$  without having its aperture obscured by the wing-pod opening. It must be light enough to allow the dual-axis gimbal designed by the University of Guelph for air-LUSI to function. It must not fail due to the repeated  $\approx 90^\circ$  C swing in temperature between the hangar and the in-flight environment.

## II. TELESCOPE OPTICAL DESIGN

### A. Overview

The design of the system is based on the instrument used in the ground-based lunar irradiance measurements of Cramer *et al.*<sup>3</sup> In the Cramer work, a commercial, off-the-shelf (COTS), 4-element apochromat telescope with a 106 mm aperture at  $f/5.0$  was used to collect light into a 50 mm diameter integrating sphere through a field stop that limited the field of view to  $\sim 1.6^\circ$ . The integrating sphere destroys the lunar image and the polarization, and an optical fiber collects radiance from the integrating sphere and sends it to a grating spectroradiometer.

The size constraints imposed by the pod preclude use of the same telescope, although a similar, COTS integrating sphere with a custom mechanical enclosure was chosen. Furthermore, the level of testing required to determine if any COTS telescope would retain its optical stability and mechanical integrity in the extreme cold environment of the ER-2 wing pod aft body, which is open to the atmosphere, was deemed prohibitive. In addition, market research could not identify a COTS telescope manufacturer that could provide a telescope that would meet flight worthiness requirements of the ER-2. The irradiance calibration methodology developed by Cramer *et al.* requires a measurement system that has a near-uniform response to an irradiance source at a range of tens of meters, preventing the use of a telescope with a central obscuration. A requirement of polarization insensitivity in the measurement system makes off-axis designs more cumbersome. Thus, a simple, custom design based on a singlet lens to collect light, and an integrating sphere to mix the light, was selected. As in the Cramer design, the moonlight from the sphere is subsequently passed to a commercial spectroradiometer via a fiber-optic bundle.



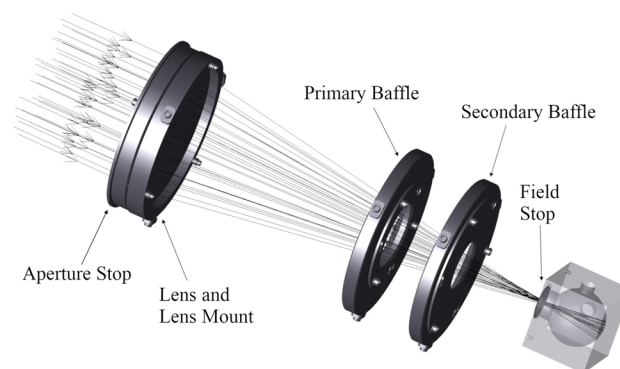
**FIG. 1.** The air-LUSI telescope with a tracking camera mounted on an astronomical telescope mount. The single lens is at the left end of the tube, and the integrating sphere is obscured at the right end. Internal details can be found in Figs. 2 and 3.

Figure 1 shows a photograph of the telescope undergoing testing at NIST's telescope calibration facility. A layout with major components and a set of rays generated by commercial ray-tracing software is shown in Fig. 2, and labels are given for major components (the optical tube is not shown). Figure 3 shows a cross section of the complete system, including the Sub-Miniature A (SMA) fiber port, which is used for collecting light into the spectroradiometer after multiple reflections from the integrating sphere wall.

In Secs. II B–II G, we go into details of the design choices.

### B. Lens size and focal length

The size scale of the telescope system is set by the diameter of the input lens and the chosen focal length. It was known from the Cramer work that a reasonable signal-to-noise ratio could be achieved with a 106 mm diameter input aperture and also that measurements could benefit from a system with a higher throughput.



**FIG. 2.** Major components of the air-LUSI telescope optical train. Optimal locations of the baffles were chosen to minimize stray light and were determined by reverse ray tracing from within the area of the field stop.

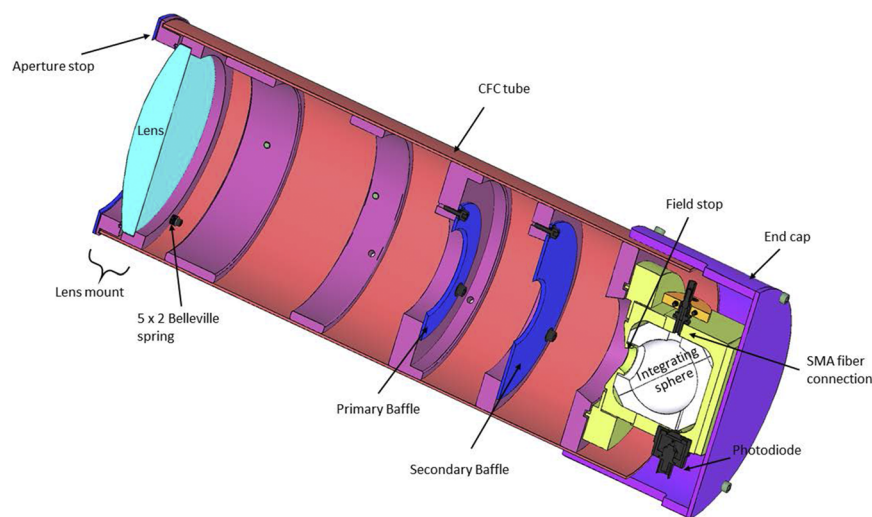


**FIG. 3.** A cutaway of the CAD model of the telescope, showing the optical train as well as the carbon fiber composite tube, the aluminum end caps, and the Invar 36<sup>®</sup> internal supports. Light is delivered to the spectroradiometer via the SMA fiber connection on the integrating sphere.

At the same time, the width of the view port on the wing pod ( $\approx 200$  mm) puts an upper limit on the diameter. An intermediate value of 139.7 mm was chosen for the lens diameter. The radius of the circular cross section wing pod ( $\approx 430$  mm) along with specific features of the gimbal mount, which has a pivot point near the center of the pod, and a requirement for space for the integrating sphere, housing, and cables at the end of the telescope constrain the focal length. After iteration with the team designing the gimbal mount, a focal length of 377 mm (corresponding to a distance of 355 mm as measured from the lens flat) was chosen at a design wavelength of 532 nm. This wavelength is chosen because the value of the index of refraction for N-BK7 corresponds to the midpoint of the value between the extrema at the ends of the wavelength range of interest ( $\sim 385$  nm and 1000 nm). The focal shift of the lens at the extrema is  $\pm 9$  mm.

### C. Field of view determination

After the single lens for the telescope is chosen, the field of view can be set by a single aperture at the entrance to the integrating sphere at the nominal focus of the lens. This aperture is known as a field stop.

The telescope's field of view needs to be large enough to accommodate the moon's diameter plus uncompensated tracking error due to aircraft movement. At the same time, the field of view should be small enough so that precise calibration of the system can be achieved in an active airplane hangar. This precise calibration can work when the field of view prevents the telescope from seeing any light originating outside of a small, black-curtain-covered structure that houses the calibration source. Furthermore, because light is collected into an integrating sphere, a smaller input port, and thus smaller field-of-view (FOV), results in higher signal. For precise calibration and maximum signal, the field of view should be large enough to track the moon, and no larger.

The average angle subtended by the moon as seen from the Earth is  $0.52^\circ$ . Because the moon's orbit is elliptical, the angle varies

from about  $0.49^\circ$  to  $0.55^\circ$ . The air-LUSI tracking system was specified to track the position of the moon to within  $0.5^\circ$  (actual tracking was found to be considerably better than this<sup>6</sup>). Since it is prudent to design for the worst case tracking, the required full angular field is two times the tracking error plus the maximum angle subtended by the moon or  $1.6^\circ$ .

The size of the field stop is straightforward to determine at the design wavelength, where a high-quality image is formed at the focus, and the field stop diameter required is  $d = 2f \tan(\theta/2) = 9.9$  mm for a back focal length  $f = 355$  mm and field-of-view (FOV)  $\theta = 1.6^\circ$ . However, away from the design wavelength, rays do not focus in the plane of the field stop, and the required aperture size must be increased so that "vignetting" does not reduce the effective FOV below the design target. In general, vignetting refers to a reduction in light intensity toward the periphery of an image, compared to the intensity at the center, caused by the blocking of light rays. A plot of vignetting for the air-LUSI telescope is shown in Fig. 4, where the fraction of unvignetted rays at 385 nm, 532 nm, and 1000 nm is plotted vs half-field angle when a 15 mm aperture is defined as the field stop. As can be seen, the 385 nm light begins to vignette when the half-field angle just exceeds  $0.8^\circ$ . At longer wavelengths, vignetting begins to occur at greater angles. The sharpness of the vignetting is maximum at the lens design wavelength where light comes to the sharpest focus and where the focus is closest to the plane of the field stop.

### D. Effects of temperature and pressure

The ER-2 aircraft cruises at an altitude of  $\sim 21$  km. Although the data acquisition system, spectroradiometer, and all supporting electronics are housed within a pressurized and temperature-controlled enclosure, the air-LUSI telescope and fiber-optic cabling are not. At this altitude, the ambient temperature and pressure will reach  $\sim -57^\circ\text{C}$  and  $\sim 5$  kPa, respectively.<sup>7</sup>

The optical system is affected by temperature in several ways. First, the index of refraction of the telescope's lens will change with temperature, and the relative index, which is measured with respect



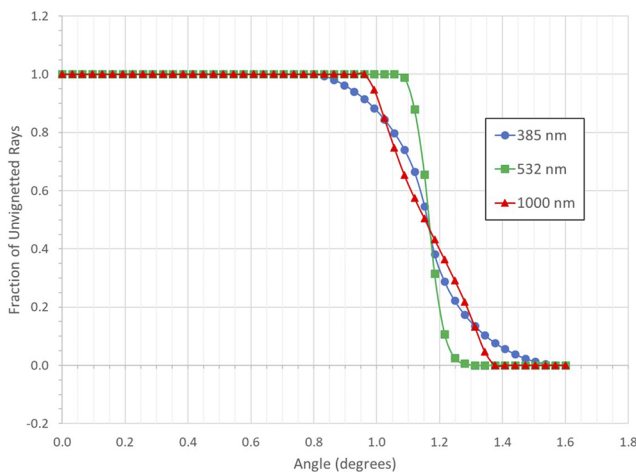


**FIG. 4.** Vignetting plot indicating the fraction of rays that enter the telescope that pass through the field stop as a function of angle.

to air, will change with pressure. Second, the glass will expand and contract with changing temperature. Third, the dimensions of the telescope housing and aperture stop, and spacing between components, will also change with temperature. To minimize the potential effects, low Coefficient of Thermal Expansion (CTE) materials were used for the telescope tube, the aperture stop, baffles, and supports, and appropriate guard bands were designed into the baffle inner diameters.<sup>8</sup> Ray traces at relevant temperatures incorporating all three of the above effects with our chosen materials show a negligible change in the system throughput with changing temperature, confirming that this important design goal is met.

In several of air-LUSI's components that can affect system throughput and calibration, there are no practical low CTE or temperature insensitive materials available. These components include the optical fiber used for the validation source, the optical fiber bundle that brings light to the spectroradiometer, and the integrating sphere at the back of the telescope. Active control of the temperature is required to maintain system performance.

To achieve control for the optical fibers, the entire bundle of fibers and wiring between the telescope and air-LUSI's pressurized and temperature-controlled enclosure are enclosed in a copper braided sleeve with heater tape. The bundle is surrounded by multi-layer insulation commonly used in aerospace applications and a fiberglass wool insulation encased in a PTFE coated fiberglass fabric that wraps in a spiral manner around the bundle and is held in place with hook-and-loop closures. A thermostat and thermocouples installed at various locations along the length are used to control and monitor the composite bundle temperature within a range of 10 °C to 20 °C.

The integrating sphere incorporates a PTFE-based reflector (Spectralon®). PTFE exhibits the highest thermal coefficient of expansion of any material used in the telescope, readily absorbs water, and is known to have a temperature-dependent response.<sup>9</sup> These material characteristics require thermal control of the integrating sphere to hold it near the same temperature at which the system is calibrated. This minimizes integrating sphere throughput

variations and prevents significant water absorption during ascent to and descent from high altitudes. A more detailed review of the telescope's material choices is given in Sec. III with a full description of the telescope's mechanical design.

The Spectralon is held in place with a 6061-T6 housing, which is coated with Anoblack Cr<sup>10</sup> to provide a low visible light reflectance to inhibit scatter near the field stop. This coating also provides a low emissivity in the infrared region (3  $\mu\text{m}$ –15  $\mu\text{m}$ ) to minimize radiative coupling to the environment. The thermal loss of the integrating sphere housing is calculated to be ~18 W based on expected conditions and is dominated by 15 W radiative losses. The temperature is controlled using a 40 W maximum output polyimide film heater controlled by a thermostat that turns the heater on at 10 °C and off at 20 °C.

The low pressure can affect the system in two ways: First, optical components, such as glasses and optical fibers, are susceptible to pressure-induced strain. These effects were considered to be too small to include in a model or to affect our calibration. Second, low air pressure results in lower heat loss to the surrounding air, which reduces the power demands on the heaters described above, and is a benefit.

## E. Baffles and stray light suppression

Stray light is defined as any light that enters the integrating sphere, which is outside the desired 1.6° full field-of-view. Any baffle placed within the interior of the telescope tube must pass the desired light cone while providing suppression of light from all other angles. Many publications containing guidelines for the location of baffles and/or vanes to suppress stray light within a telescope may be found in the literature. A small sampling of such appears in the work of Breault,<sup>11</sup> Cheng,<sup>12</sup> and Leinert and Klüppelberg.<sup>13</sup> The guidelines are implemented here for initial baffle placement in a computer model, followed by brute-force “reverse” ray tracing to determine optimal locations. This approach incorporates individual assignments of reflectance and scattering properties of telescope components and allows direct assessment of the impact of component design on stray light-suppression.

The use of reverse ray tracing relies on Helmholtz reciprocity,<sup>14</sup> which is the principle that a ray propagating in a forward fashion encounters the same reflections and refractions as its time-reverse. To determine the amount of stray light that enters the integrating sphere, rays can be traced as if they are emitted from within the integrating sphere aperture. Figure 5 illustrates one step in the reverse ray trace used to determine optimum baffle location within the air-LUSI telescope. This particular trace incorporates no internal baffles. In Fig. 5(a), a virtual source that radiates light into a hemisphere is placed at the sphere aperture. The direction of the source is away from the sphere. An unscattered portion of the light will propagate directly through the lens, and another portion will strike the inside wall of the tube and scatter in many arbitrary directions. Along with the unscattered light, the scattered light eventually exits the tube as shown and strikes a virtual detector at the output of the tube. The irradiance at the virtual detector is shown in false color on a log scale. The irradiance consists of a central core corresponding primarily to the unscattered portion of light, and the surrounding “haze” is due to the scattered portion. The result of this technique is shown in Figs. 5(b) and 5(c) for unscattered and scattered flux, respectively.

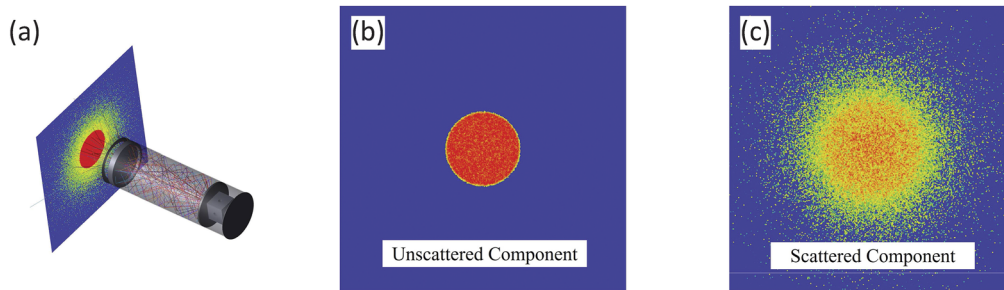


**FIG. 5.** A schematic of the reverse ray tracing to determine stray light. Baffles are not included in this simulation. In panel (a), the telescope and tube assembly are shown, with rays traced from the field stop into a hemisphere and scattering off of the tube or directly impacting the virtual detector square at left. The density of rays in the virtual detector is indicated by the color, with dark red being the densest. Panel (b) shows the density of rays that have impacted the virtual detector without any scattering, while panel (c) shows the rays that impact the virtual detector after at least one reflection from another surface.

By taking the ratio of the scattered flux to the total flux, a stray light contribution metric can be formed. In the next step, a virtual baffle with a known inner diameter is introduced. Ray traces are performed as it is moved along the inside length of the tube starting from the sphere, as shown in the upper right-hand corner of Fig. 6, subject to the constraint that its inner diameter cannot be allowed to intersect the light cone corresponding to the desired field-of-view. A plot of the stray light contribution metric as a function of position along the tube and inner baffle diameter is shown in Fig. 6. All internal walls were assigned a reflectance of 2% with a Lambertian scattering profile. A minimum in the stray light contribution was found for a primary baffle having an inner diameter equal to 57 mm located at 140 mm from the sphere entrance port. To provide a small guard band, the actual baffle inner diameter was selected to be 60 mm. An additional, secondary baffle was introduced between the primary

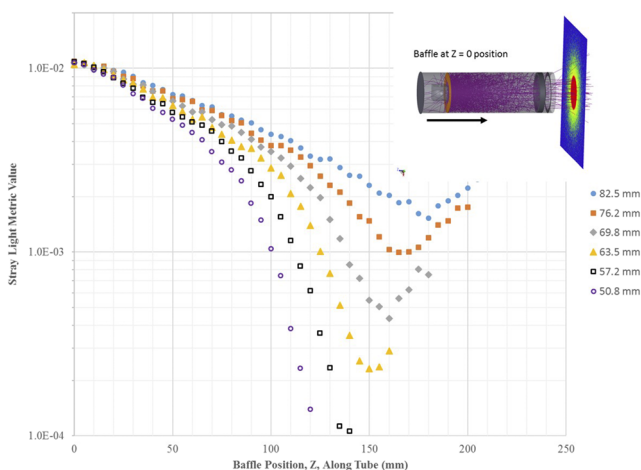


**FIG. 6.** Value of a fitness function, defined as the ratio between the amount of reverse-ray-traced light that has been scattered before hitting an external virtual detector to the amount that directly hits the virtual detector with no scattering (see Fig. 5), as a function of baffle location for a set of six different baffle internal diameters (indicated in the legend at right).

baffle and field stop. Its location and inner diameter were optimized following the same procedure to provide further stray light rejection.

Finally, optical black coatings are important to the control of stray light. Pompea and Breault<sup>15</sup> gave a comprehensive review of traditional paints, coatings, and processes for generating black surfaces. Due to cost and time constraints, and relative ease of application, Aeroglaze® Z306<sup>16</sup> was selected as the black coating applied to all interior surfaces of the air-LUSI telescope. Z306 advantages include durability, low outgassing, and a history of successful use in aerospace applications.

## F. Expected throughput to spectroradiometer

A 50.8 mm diameter integrating sphere collects and mixes the moonlight before its introduction to the spectroradiometer via the fiber-optic bundle that samples the sphere wall radiance. Since the sphere spatially mixes the light, the signal fed to the spectroradiometer is robust against shifts in the light pattern at the entrance port of the sphere as the telescope tracks the moon. This is an advantage over more direct coupling methods. However, a disadvantage is a severe reduction in optical throughput. Low throughput requires multi-second spectroradiometer integration times and averaging to achieve good signal-to-noise ratios. Thus, care should be taken in the sphere design to ensure that throughput is optimized.

To illustrate the throughput challenge, consider the calculation of the optical flux,  $\Phi$ , collected by the bundle during flight. An auxiliary measurement of the radiance responsivity of the spectroradiometer when the bare fiber bundle is looking at a radiance source gave a responsivity of 5600 digital counts per  $\mu\text{W cm}^{-2} \text{ nm}^{-1} \text{ sr}^{-1} \text{ s}^{-1}$  at 550 nm, where the full scale of the spectroradiometer is  $2^{15}$  digital counts. To estimate the radiance that the spectroradiometer will measure in the integrating sphere at the back of the telescope, we start with the equation for the radiance of the sphere wall for an ideal integrating sphere with Lambertian reflectivity on the walls,<sup>17</sup>

$$L_s = \frac{\phi_i}{\pi A_s} \left[ \frac{\rho}{1 - \rho(1 - f)} \right], \quad (1)$$

where  $\phi_i$  is the incident flux,  $A_s$  is the interior surface area of the sphere,  $\rho$  is the reflectance of the sphere wall, and  $f$  is the port

fraction defined by the sum of all open port areas divided by  $A_s$ . The fraction within the brackets is a dimensionless quantity referred to as the sphere multiplier,  $M$ . In air-LUST's sphere, there are four ports: the entrance port (field stop), 15 mm in diameter; two fiber-optic ports each  $\sim 3$  mm in diameter; and one monitor photodiode port about 1 mm in diameter. Assuming a nominal reflectance  $\rho = 0.99$  for the sphere wall (corresponding to a typical diffuse reflectance of Spectralon<sup>18</sup>), the value  $M = \frac{0.99}{[1 - 0.99(1 - 0.0236)]} \approx 30$ . Note that this number varies rapidly with small changes in the mean surface reflectance of the sphere.

To complete the estimate of  $L_s$  during flight, Table 1 of Ref. 3 gives values for the top-of-atmosphere (TOA) spectral irradiance between 450 nm and 1000 nm over a sun-moon-observer angle (i.e., lunar phase) ranging from  $17^\circ$  to  $20^\circ$ . At 550 nm, the TOA spectral irradiance is about  $2.6 \times 10^{-4} \mu\text{W cm}^{-2} \text{ nm}^{-1}$ . The diameter of the aperture stop is 127 mm, and its area is about  $0.0127 \text{ m}^2$ ; thus, the flux entering the sphere at 550 nm is  $0.033 \mu\text{W nm}^{-1}$  (ignoring reflection losses). Since the internal surface area of the sphere is  $\sim 8100 \text{ mm}^2$  and  $M = 30$ , the radiance on the sphere wall is  $L_s \approx 3.9 \times 10^{-3} \mu\text{W cm}^{-2} \text{ sr}^{-1} \text{ nm}^{-1}$  at 550 nm. Then, combining this with our measurement of the radiance responsivity of the spectroradiometer, we estimate a count rate of  $\approx 3100 \text{ counts s}^{-1}$  at 550 nm, meaning that a good signal-to-noise ratio can be achieved with integration times in the range of several seconds. This compares to the observed count rate of about  $2000 \text{ counts s}^{-1}$  in our laboratory calibrations using an irradiance of  $3.1 \times 10^{-4} \mu\text{W cm}^{-2} \text{ nm}^{-1}$ , indicating that the system performs nearly as expected (Note that because of the extreme dependence of the sphere multiplier on small changes in reflectivity and port fraction, estimates of sphere throughput are not precise).

The diameter of the field stop could be reduced because the tracking is well within  $0.5^\circ$ . Since the field stop is the sphere entrance port, any reduction in size lowers the port fraction, causing the sphere multiplier to increase and increasing throughput. The practical result would be a reduction in required spectroradiometer integration time to achieve a given signal-to-noise ratio. However, higher sphere multipliers result in more sensitivity to small changes in the sphere's physical characteristics, so pushing the multiplier too high may affect measurement uncertainty.

### G. Optical design validation

The telescope was set up in the NIST telescope calibration facility<sup>19,20</sup> to view the 100 mm diameter exit port of a 30 cm diameter, Spectralon integrating sphere illuminated by using a Quartz-Tungsten-Halogen (QTH) source operating at a correlated color temperature of  $\sim 3200 \text{ K}$ . The telescope's entrance aperture was located 11 m from the 100 mm port. This combination of source size and distance from the telescope produces a source subtense approximately equal to that of the full moon.

For the first test, the telescope's integrating sphere was removed so that the image of the source's 100 mm port at the telescope field stop could be examined. A fixed focal length macrolens having unity magnification was coupled to a digital Single Lens Reflex (SLR) camera to relay the image at the field stop to the camera's imaging sensor. Figure 7(a) shows the resulting image at the camera's  $22.4 \times 14.8 \text{ mm}^2$  imaging sensor. The image is out of focus for two reasons: (1) the source is at a relatively small and finite

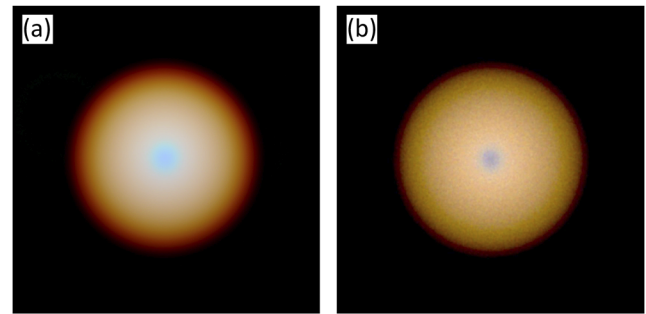


FIG. 7. A comparison of a camera image (a) of a 100 mm diameter QTH sphere source viewed through the telescope with a simulation of the same setup (b).

distance from the telescope and (2) the aberrations produced by the telescope's simple Plano-ConveX (PCX) lens are not corrected. Figure 7(b) shows the predicted image for a 3200 K source as generated by the OpticStudio design model working in non-sequential mode with a "true color"  $22.4 \times 14.8 \text{ mm}^2$  virtual detector. As can be seen, the size and color of the camera image, and model prediction, are similar, with a central blue peak and a diffuse red edge. The slight variation observed may be due to the spectral transmission of the anti-reflection coating deposited on the macrolens, which is not known and not modeled, as well as the spectrally varying throughput of the source integrating sphere.

For the second test, the field-of-view of the telescope was measured. The camera and macrolens were removed, and the telescope's integrating sphere was re-installed. The telescope was attached to a computerized commercial telescope mount to facilitate precise rotation of the telescope about one axis. In this case, the source distance was 14.2 m from the telescope entrance aperture. The output of the optical fiber that monitors the sphere wall radiance was coupled to the spectroradiometer, and the collected flux vs wavelength and rotation angle was measured. Since the source is relatively close to the

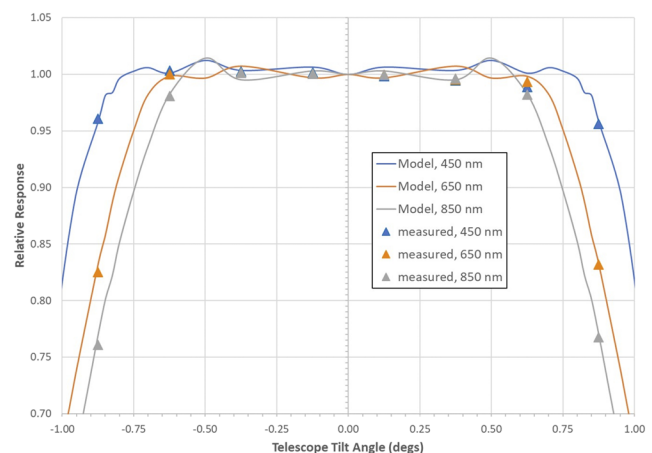


FIG. 8. Modeled and measured throughput of the telescope as a function of angle when viewing a point source at 14.2 m from the entrance aperture.



telescope, the expected FOV should be less than that predicted for the moon. The results are shown in Fig. 8. The solid lines are the model prediction, and the triangles are the measured values. As can be seen, the agreement is very good. In this case, the anti-reflection coating deposited on the telescope's lens was accounted for because its design is known.

### III. MECHANICAL DESIGN

The mechanical design of the telescope was developed considering the environmental conditions present in an open-air cavity of an aircraft that ascends to 21 km where it cruises for ~1 h before descending. The accelerations, temperature fluctuations, vibrations, and pressure changes all must be considered in order to ensure reliable operation at altitude as well as in the hangar for pre- and post-flight calibration. As stated previously, the design relies on low CTE materials to maintain dimensional stability over the greater than 90 °C temperature range the telescope encounters during a 2-h mission.

When assembled, the telescope is ~468 mm long. The telescope's shell is a 152.4 mm ID carbon fiber composite (CFC) tube with 1.37 mm thick wall. The manufacturer describes the material as "convolute wrapped 3 k 8 harness satin weave with a fiber orientation of 0°/90° and a fiber/resin ratio of 60%/40% by weight."<sup>21</sup> The tube is 406 mm in length and houses seven Invar 36® rings to provide mechanical support for the lens, the pointing camera, tracking system coupling, optical baffles, and the integrating sphere. The rings were heat treated post-machining to provide both stress relief and dimensional stability.<sup>22</sup> All of the fasteners used in the construction of the telescope, as well as the whole air-LUSI instrument, were either military specification (MS) or National Aerospace Standard (NAS) certified in order to meet the requirements of the ER-2 Experimenter handbook.<sup>23</sup> In addition, all fasteners in the telescope required locking features; in most cases, these were locking threaded inserts or all-metal flex-top type locknuts to ensure fasteners resisted loosening during flight. Furthermore, blind tapped holes were avoided as often as possible or vented if necessary to avoid any trapped air and any effects that may have on the fastener's stability. The rings are each attached to the CFC tube with three radial fasteners seated in a saddle washer to compensate for the curvature of the tube. All of the fabricated components in the telescope (rings, baffles, saddle washers, and the CFC tube) were roughened (CFC tube by hand sanding and metal components by bead blasting) and painted with Aeroglaze Z306, as previously stated, to provide a low scatter optical black surface, to seal out moisture, and to prevent corrosion.

The telescope's lens is captured between two rings with the addition of a silicone O-ring and stretch polyester gasket to provide a soft seat for the lens. The former accommodates any asymmetry in the lens preload on the lens' curved front surface, and the latter compensates for any roughness in the machined seat for the flat rear surface of the lens. The lens mount preload requirement of ~750 N was determined using ER-2 Experimenter handbook requirements and the sag of the lens at its mounting point.<sup>24</sup> The preload is provided by three 5 × 2 Belleville disk spring stacks compressed with 4–40 socket head cap screws to capture the lens and keep it secure during flight vibrations. This configuration allowed for simple assembly and removal in the field if lens replacement would be required between

flights. The baffles and entrance aperture are also made of Invar 36 and are bolted directly to the face of support rings within the telescope. The rear end of the telescope is capped with a slotted cap fabricated from 6061-T6 and attached to the rearmost ring of the telescope. The cap provides protection from dust and debris during flight as well as provides a mechanical barrier to guard the electrical and optical connectors on the integrating sphere housing.

The integrating sphere is kinematically coupled to the telescope's rear ring to allow for simple removal and replacement for alignment and calibration. The lens, baffles, and integrating sphere aperture have been aligned in a NIST laboratory to ensure that the centerline of each aperture is coincident with the centerline of the lens. This was accomplished by aligning a laser centered and normal to the telescope's lens and using reticules mounted on the center of the baffle to center the baffles to the beam. Finally, the integrating sphere with its integral field stop is aligned with the same laser beam in a similar fashion, yielding the optical system with apertures aligned to the centerline of the telescope lens.

The integrating sphere assembly includes a 15 mm diameter entrance aperture/port, which is the system's field stop, to accommodate the  $\pm 0.5^\circ$  pointing error window mentioned previously. The integrating sphere also contains three additional ports: Two of the ports utilize SMA threaded couplings to facilitate fiber coupling of an LED validation source and the spectroradiometer. The third port is directly coupled to a silicon photodiode for monitoring of the optical signal level during measurements and calibrations of the instrument.

### IV. CONCLUSION

In order to meet the requirements of the air-LUSI mission, to measure the spectral irradiance of the moon with high-precision from a high-altitude platform, NIST has developed a non-imaging telescope capable of enduring extreme temperature and pressure swings with minimal changes to its throughput. The telescope's optical and mechanical design is based on the need to fit within the NASA ER-2 wing pod and on the environmental demands. Laboratory testing confirmed that the as-built telescope performance closely matches the performance predicted by the optical modeling of the system.

The air-LUSI team is preparing a manuscript detailing the full air-LUSI system including the motion control, environmental, electronic, and radiometric systems.<sup>5</sup> To date, the air-LUSI instrument has successfully flown seven times during two deployments (Summer 2018 and Fall 2019) and has recorded preliminary lunar irradiance measurements that are currently under evaluation by NIST as well as end-users of the data.

Once data for record are obtained, NIST is hopeful that air-LUSI will provide lunar spectral irradiance measurements that will help improve the uncertainties of the existing models used to estimate the lunar irradiance and improve the moon's utility as an on-orbit calibration source.

### ACKNOWLEDGMENTS

The authors gratefully acknowledge funding for this work from NASA's Airborne Instrument Technology Transfer program under

Grant No. 80NSSC17K0495 and support from NASA's Armstrong Flight Center. They would also like to acknowledge contributions to this work from Marc Mogavero, HAWK Institute for Space Sciences, and Andrew Cataford, University of Guelph.

## DATA AVAILABILITY

The data that support the findings of this study are available from the corresponding author upon reasonable request.

## REFERENCES

- <sup>1</sup>T. C. Stone, private communication (2017).
- <sup>2</sup>T. C. Stone, H. Kieffer, C. Lukashin, and K. Turpie, "The moon as a climate-quality radiometric calibration reference," *Remote Sens.* **12**, 1837 (2020).
- <sup>3</sup>C. E. Cramer, K. R. Lykke, J. T. Woodward, and A. W. Smith, "Precise measurement of lunar spectral irradiance at visible wavelengths," *J. Res. Natl. Inst. Stand. Technol.* **118**, 396–402 (2013).
- <sup>4</sup>C. E. Cramer, G. T. Fraser, K. R. Lykke, A. W. Smith, and J. T. Woodward, "A novel apparatus to measure reflected sunlight from the Moon," *Proc. SPIE* **8867**, 271–279 (2013).
- <sup>5</sup>K. R. Turpie, S. Brown, J. T. Woodward, S. A. Gadsden, T. C. Stone, S. E. Grantham, T. C. Larason, S. E. Maxwell, R. E. Eplee, A. Cataford, Jr., and A. Newton, "The airborne lunar spectral irradiance (air-LUSI) mission: An overview" (unpublished).
- <sup>6</sup>A. Cataford, S. A. Gadsden, K. Turpie, and M. Biglarbegian, "Air-LUSI: Estimation, filtering, and PID tracking simulation," in *2018 IEEE Canadian Conference on Electrical Computer Engineering (CCECE)* (IEEE, 2018), pp. 1–6.
- <sup>7</sup>U.S. Standard Atmosphere, 1976, NOAA - SIT 76-1562, National Oceanic and Atmospheric Administration, 1976.
- <sup>8</sup>P. Yoder and D. Vukobratovich, "Opto-mechanical characteristics of materials," *Opto-Mechanical Systems Design*, 4th ed. (CRC Press, 2015), Vol. 1.
- <sup>9</sup>C. P. Ball, A. P. Levick, E. R. Woolliams, P. D. Green, M. R. Dury, R. Winkler, A. J. Deadman, N. P. Fox, and M. D. King, "Effect of polytetrafluoroethylene (PTFE) phase transition at 19°C on the use of Spectralon as a reference standard for reflectance," *Appl. Opt.* **52**, 4806–4812 (2013).
- <sup>10</sup>See <https://www.anoplate.com/media/1222/anoblack-cr-final-1-24-18.pdf> for Anoplate Corporation, Technical data sheet AnoBlack Cr.
- <sup>11</sup>R. Breault, "Control of stray light," *Handbook of Optics*, 2nd ed. (McGraw-Hill, 1995), Vol. I, pp. 38.1–38.35.
- <sup>12</sup>J. Cheng, "The principles of astronomical telescope design," in *The Principles of Astronomical Telescope Design*, Astrophysics and Space Science Library (Springer-Verlag, New York, 2009), pp. 135–139.
- <sup>13</sup>C. Leinert and D. Klüppelberg, "Stray light suppression in optical space experiments," *Appl. Opt.* **13**, 556–564 (1974).
- <sup>14</sup>T. A. Germer, J. C. Zwinkels, and B. K. Tsai, "Chapter 2—Theoretical concepts in spectrophotometric measurements," in *Experimental Methods in the Physical Sciences, Spectrophotometry*, edited by T. A. Germer, J. C. Zwinkels, and B. K. Tsai (Academic Press, 2014), Vol. 46, pp. 11–66.
- <sup>15</sup>S. Pompea and R. Breault, "Black surfaces for optical systems," in *Handbook of Optics*, 2nd ed. (McGraw-Hill, 1995), Vol. I, pp. 37.1–37.70.
- <sup>16</sup>M. J. Persky, "Review of black surfaces for space-borne infrared systems," *Rev. Sci. Instrum.* **70**, 2193–2217 (1999).
- <sup>17</sup>See [https://www.labsphere.com/site/assets/files/2551/integrating\\_sphere\\_theory\\_apps\\_tech\\_guide.pdf](https://www.labsphere.com/site/assets/files/2551/integrating_sphere_theory_apps_tech_guide.pdf) for Technical Guide: Integrating Sphere Theory and Applications, Labsphere, Inc.
- <sup>18</sup>See <https://www.labsphere.com/site/assets/files/2553/a-guide-to-reflectance-materials-and-coatings.pdf> for Technical Guide: Reflectance Materials and Coatings, Labsphere, Inc.
- <sup>19</sup>See <https://www.nist.gov/laboratories/tools-instruments/telescope-calibration-facility-tcf> for NIST Telescope Calibration Facility (TCF).
- <sup>20</sup>A. W. Smith, J. T. Woodward, C. A. Jenkins, S. W. Brown, and K. R. Lykke, "Absolute flux calibration of stars: Calibration of the reference telescope," *Metrologia* **46**, S219–S223 (2009).
- <sup>21</sup>See <https://publicmissiles.com/product/composites> for additional information about carbon fiber composites and their properties; accessed 11 February 2020.
- <sup>22</sup>B. Lement, B. Averbach, and M. Cohen, "The dimensional behavior of Invar," *Trans. Am. Soc. Met.* **43**, 1072–1097 (1951).
- <sup>23</sup>See [https://www.nasa.gov/centers/dryden/pdf/90464main\\_ER2handbook.pdf](https://www.nasa.gov/centers/dryden/pdf/90464main_ER2handbook.pdf) for NASA Dryden Flight Research Center, ER-2 Airborne laboratory experimenter handbook.
- <sup>24</sup>P. Yoder and D. Vukobratovich, "Mounting individual lenses," *Opto-Mechanical Systems Design*, 4th ed. (CRC Press, 2015), Vol. 1.